Article

Characterization of Microstructure and High Temperature Compressive Strength of Austenitic Stainless Steel (21-4N) through Powder Metallurgy Route

Arun Prasad Murali [1], Dharmalingam Ganesan [1], Sachin Salunkhe [1,*], Emad Abouel Nasr [2],
João Paulo Davim [3] and Hussein Mohamed Abdelmoneam Hussein[4,5]

1 Department of Mechanical Engineering, Vel Tech Rangarajan Dr. Sagunthala R & D Institute of Science and Technology, Chennai 600062, India; arunprasadm@veltech.edu.in (A.P.M.); gdharmalingam@veltech.edu.in (D.G.)
2 Industrial Engineering Department, College of Engineering, King Saud University, Riyadh 11421, Saudi Arabia; eabdelghany@ksu.edu.sa
3 Department of Mechanical Engineering, Campus Universitário de Santiago, University of Aveiro, 3810-193 Aveiro, Portugal; pdavim@ua.pt
4 Mechanical Engineering Department, Faculty of Engineering and Technology, Future University in Egypt, New Cairo 11835, Egypt; hussein.hussein@fue.edu.eg
5 Mechanical Engineering Department, Faculty of Engineering, Helwan University, Cairo 11732, Egypt; hussein@h-eng.helwan.edu.eg
* Correspondence: drsalunkhesachin@veltech.edu.in

Abstract: Exposure of the engine valve to high temperatures led to the degradation of the valve material due to microstructural instability and deteriorating mechanical properties. Performance enhancement and alteration in microstructures can be attained through the powder metallurgy route which is a viable method to produce near net shape components. In this current study, the development of austenitic stainless steel (21-4N) through the powder metallurgy route as an alternate material for engine valves was investigated. Mechanical alloying was carried out for the pre-alloyed mixtures and consolidated using vacuum hot pressing. Sintering parameters were fixed at 1200 °C, 50 MPa and at a vacuum level of 10-3 Torr. A scanning electron microscope was used to analyze the morphology of the milled powders. Densities for the hot pressed powders were compared with theoretical densities and found to be around 98–99%. Observations regarding grain size, the presence of austenitic grain, heterogeneous distribution of metal carbides and analysis of chemical composition along the metal matrix were determined using both optical and electron microscopes. X-ray diffraction was carried out for both the consolidated and powder samples. The hot pressed samples exhibited a hardness value of 410 ± 10 Hv. An isothermal compression test for the sintered samples was carried out at a temperature of 650 °C and strain rate of 0.001 s^{-1}. It is showed that the compressive strength of 1380 MPa. An analysis between the room temperature yield strength obtained from hardness measurement and the strengthening mechanism based on the microstructure was conducted. Grain size, dislocation and solid solution are the major strengthening mechanisms which strengthen the material. Overall, the development of valve steel material through the powder metallurgy route exhibited improved metallurgical and mechanical properties in comparison to the corresponding cast product.

Keywords: 21-4N valve steel; mechanical alloying; vacuum hot pressing; powder metallurgy

1. Introduction

Almost all engine valves consist of bi-metallic welded materials, which are composed of hardened steel stem and a superalloy. Superalloys previously used for valve manufacturing include Inconel 751, Pyromet 31 and Nimonic 80A which are resistant to heat, oxidation/corrosion and wear at elevated temperatures [1]. Due to the higher cost and

processing requirements of nickel-based superalloys, valve manufacturers initiated the development of an alternate material consisting of titanium and austenitic stainless steels (21-4N). Due to the low density of titanium alloys, it had a good strength to weight ratio when compared to existing materials consisting of nickel superalloys. However, titanium alloys had poor room temperature ductility, low toughness properties and a high cost of production [2]. An alternate suitable material to improve strength, resistance to creep, corrosion and oxidation resistance at elevated temperatures is 21-4N austenitic heat resistant stainless steel [3]. It consists of a high chromium and manganese content which improve the material properties and provide structural stability. The high pressure and high operating temperature of automotive valves ranges between 800–950 °C, where the instability in strength was noted [4].

Zhang et al. analyzed the failure of valve heads due to the non-uniform distribution of temperature in the valve region, which resulted in an increased stress concentration and led to a crack in valve heads [5]. Similarly, a review of the failure of the engine valve conducted by Naresh et al. suggested that the principal reason for the failure of the valve is excessive heating leading to the degradation of valve material, fretting, microstructural instability and impact load [6]. If the engine valve is deemed poor, the output power decreases or can even lead to seizure. Overall, analyses regarding automotive failure have been conducted predominantly in engines [7].

Several researchers carried out the failure analysis of engine valves and interpreted the cause for its failures. Yu et al. investigated the failure of an exhaust valve made of 5Cr21Mn9Ni4N steel. It was stated that the reason for the failure is the disintegration of the austenitic structure due to the depletion of chromium from the grain structure. This led to impaired mechanical properties and subsequently fatigue failure [8]. Kum et al. found that the thermal deformation of valve heads leads to valve fracture. Moreover, they found that fractures occurred as a result of non-uniform stress distribution near the valve region [9].

Overall, it can be seen that materials produced through the cast route showed inhomogeneous grain growth throughout the product due to the uneven solidification rate during the casting process. To overcome these defects, alloys were developed through directional solidification to uplift the mechanical properties along the longitudinal directions. This will eliminate the weakening of the grain boundary and enhance high temperature mechanical strength. One such method to obtain high strength with fine grain structure is the powder metallurgy route. Near net shapes are obtained using the powder metallurgy process which reduces secondary machining processes such as milling, turning and drilling [10,11]. A better surface finish, close tolerance and post or secondary processing are needed for many parts in the service industry. With the introduction of powder metallurgy components, market review shows that 60% of components will only require one machining processes [12]. Powder consolidation techniques using vacuum hot pressing will eliminate unwanted and undesirable reactions within metal matrices due to the lower processing temperature [13]. Great flexibility during material design and selection can be achieved using powder metallurgy technique. Due to these advantages, materials developed using the powder metallurgy route exhibit superior properties in comparison to their counterparts developed through traditional methods such as the melting and casting route [14–16]. Components produced through the powder metallurgy route present fine microstructure and a homogeneous distribution of particles [17]. To consolidate metal powder particles in order to attain superior strength, hot pressing under vacuum conditions was carried out. During this process, both temperature and pressure were applied to the powder compacts. Vacuum condition was used to provide control over the atmosphere to prevent oxidation at a high temperature. These powder particles consist of a single phase before consolidation. It is attained by the process of mechanical alloying (MA). Without melting, the solid solution can be attained by violently deforming the powder mixtures under controlled conditions. This non-equilibrium process works based on energizing and quenching, whereby the alloyed materials are brought into the metastable state with the application of pressure and temperature. Moreover, studies related to hot compression for 21-4N were carried out

previously using the casting route [18–20], whereas hot compression studies of 21-4N steel developed using the powder metallurgy route have yet to be reported.

The literature related to the comparison of mechanical and microstructural properties of similar materials with different processing routes are relatively scarce. Bartolomeu et al. studied the microstructure and mechanical properties of austenitic 316L stainless steel developed using both conventional casting and also the powder metallurgy route (hot pressing). It was reported that 316L stainless steel samples had a coarse grain structure in cast route whereas they possessed an equiaxed grain structure when developed using the hot pressing technique. A slight increase in hardness of 6% was reported for 316L developed through hot pressing. Yield and tensile strength increased by 33% and 50%, respectively, due to the equiaxed grain structure [14]. Garbacz et al. compared the mechanical and microstructural properties of platinum and rhodium (Pt-Rh) alloys manufactured using the isostatic pressing and casting route. When subjected to tensile testing, both the alloys exhibited an increase in tensile property by a factor of 2.5 when compared to alloys manufactured using the casting technique. The increase in tensile properties for Pt-Rh alloys developed using the powder metallurgy route can be attributed to grain size strengthening as a result of the fine grain size when compared with the coarser grain obtained with the casting route [15]. High entropy alloys consisting of Fe-Ni were developed by Larissa et al. using the cast and spark plasma sintering technique. Alloys developed using powder metallurgy possessed a nano-sized FCC metal matrix with a uniform and fine grained microstructure, whereas in contrast, cast alloys showed a coarse grained structure. Similarly, the mechanical properties were far superior when compared to its cast products [16]. Overall, the alloys developed through the powder metallurgy route showed improved mechanical properties when compared to cast products of a similar composition.

In the present work, we developed a suitable substitute for valve materials consisting of austenitic stainless steel (21-4N) using the powder metallurgy technique. It is very important that the microstructural stability of the material is evaluated using an optical micrograph (OM), scanning electron microscope (SEM) along with energy dispersive spectrum (EDS) and transmission electron microscopy (TEM) studies. The structural evolution of the powders was studied using SEM, and the X-ray diffraction (XRD) patterns were also evaluated for the hot pressed samples. The Vickers hardness (HV) for the consolidated samples was evaluated and compared with results obtained with various strengthening mechanisms.

2. Experimental Procedures

The chemical composition for the valve material of 21-4N austenitic stainless steel was developed with ferro-alloy powders of Fe-Ni, Fe-Mn and Fe-Cr which had a particle size of less than 25 μm. The desired chemical composition of 21-4N heat resistant steel is shown in Table 1.

Table 1. Individual elemental composition for 21-4N steel.

Alloy	Concentration of Elements in wt%					
	Cr	**Ni**	**Mn**	**C**	**Si**	**Fe**
21-4N	21	4	8.2	0.48	0.40	Rest

To convert the pre-alloyed mixtures into austenitic alloy, high energy planetary ball milling was used. MA was executed in a Fristch GmbH planetary ball mill with tungsten carbide balls and vials where the ball to powder ratio (BPR) was 10:1. Ball milling was carried out for 10 h at 300 rpm with toluene as the process control agent. The structural morphology of the milled powders at regular intervals were studied using SEM analysis. Milled powders were consolidated using vacuum hot pressing with a temperature, pressure and vacuum level of 1200 °C, 50 MPa and 10^{-3} Torr, respectively, for a period of 2 h. A schematic representation is shown in Figure 1 for vacuum hot pressing. After vacuum hot

pressing, the dimensions of the consolidated sample obtained were 30 mm in diameter and 12 mm in height as shown in Figure 2.
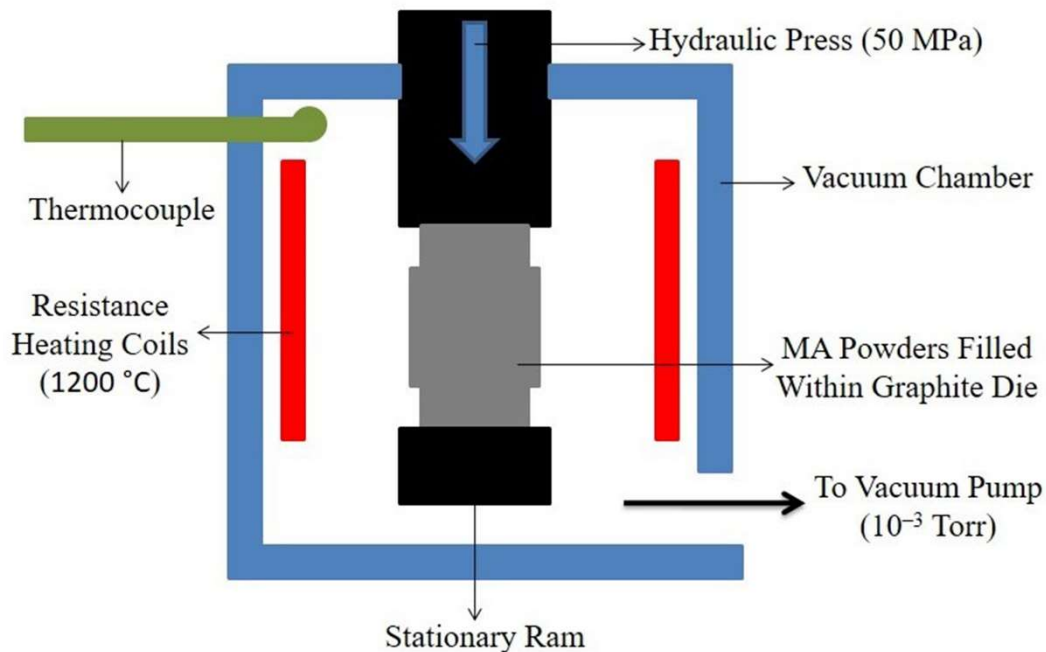

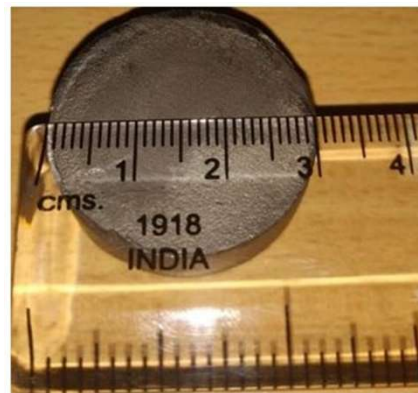**Figure 1.** Schematic representation of vacuum hot pressing.

Figure 2. Schematic representation of vacuum hot pressed sample.

Vacuum hot pressed samples were analyzed for densification studies, microstructural examination and phase determination. Metallographic techniques were used to prepare the sample with ferric chloride as the etchant to reveal the microstructure. The phase distribution, shape and morphology of both powder and vacuum hot pressed samples were studied using SEM-EDS. INCA Xsight JOEL–JEM–2100 was used to carry out the transmission electron microscopy (TEM) study operated at 200 kV. The preparation of samples for TEM studies was initially carried out with Gatan model 656 for dimpling the specimens, followed by ion milling with Gatan model 691. Measurement of hardness for the hot pressed samples was evaluated at room temperature in a Vickers micro hardness tester using a FIE Model OMEGA hardness tester (Deckenpfronn, Germany). Indentation was carried out using a diamond intender at a load of 1 kg for a dwell time of 15 s. The bottom of the test specimens were filed flat before each testing. From each of the three hot pressed samples, 10 indentations were carried out and each of the indents were spaced 3 mm from each other. Zwick/Roell Z100 was used to carry out compression testing to evaluate the compression strength of the hot pressed samples as per ASTM E209, with a strain rate of

0.001 s^{-1} and at 650 °C. Specimens of cylindrical sizes with a height 10 mm and diameter 8 mm were subjected to uniaxial compression. During hot compression, the sintered samples were heated through resistance heating and the temperature measurements were conducted in thermocouples. To reduce the effect of friction during hot compression, the two ends of the sample were padded with a lubrication sheet consisting of graphite.

3. Results and Discussion

3.1. Structural Morphology of Milled Powders

Pre-alloyed mixtures of the powder particles consisting of ferro-alloys and traces of elemental powders that were blended inside a tungsten carbide vial are shown in Figure 3a. From the micrograph, it can be observed that the ferro-alloy particle mixtures consisted of various shapes such as irregular dentritic and flaky structures. Similarly, the morphology of the mixtures is shown in Figure 3b,c for a milling condition of 5 h and 10 h, respectively.
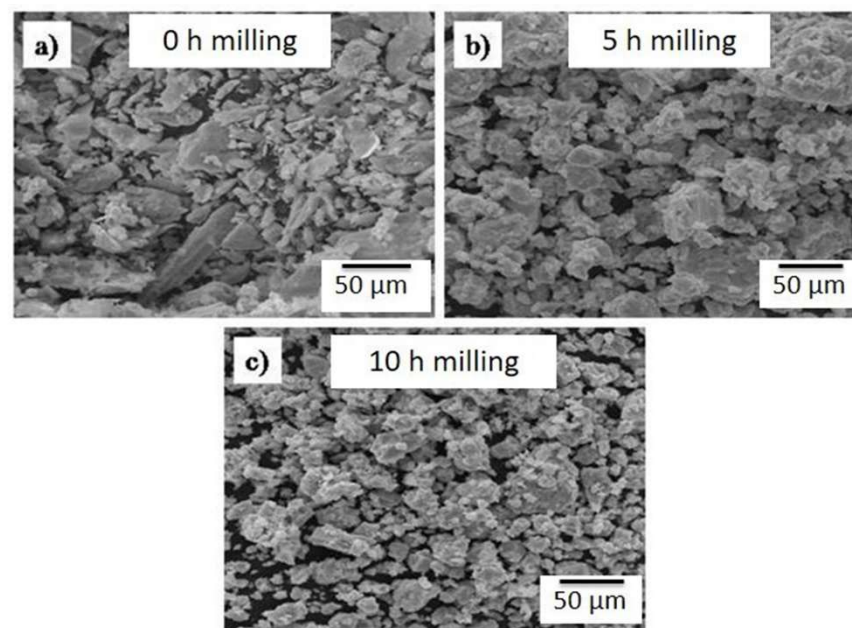
Figure 3. (**a**–**c**) Morphology of milled powders at regular milling interval.

From the SEM morphology, significant variations in size and morphology of the pre-alloyed powders during the entire milling time at regular intervals can be observed. The initial condition of the powder particles was soft and ductile. As the milling was carried out in wet conditions, these soft particles tended to agglomerate with each other during the early stages. With the continuation of milling, the agglomerated particles break down and flatten. It is evident that the milled powders are finer when compared to the initial condition after 5 h of milling. The formation of finer particles is due to the repeated fracturing and welding between the powder particles due to collisions between ball-powder-vial. Due to the high impact ball-powder-vial and shearing action between them, a high amount of energy was transferred to the milled powders. However, after 10 h of milling, the milled powders were found to be fragmented due to continuous work hardening. The surface properties revealed that the fracturing of the powder particles was dominant when compared to cold welding.

From Table 2, several studies carried out on the formation of austenitic stainless steel through MA are presented and it can be inferred that the formation of austenitic stainless steel depends on the milling parameters, namely starting materials, milling medium, BPR and milling time.

Table 2. Evolution of various austenitic grade stainless steels from different starting powders through MA.

Elemental/Pre-Alloyed Mixtures	Balls and Vial	BPR	Milling Speed (rpm)	Milling Time (h)	References
304, 316 and 310	Stainless Steel	5:1	300	50	[21]
Fe, Cr, Ni and W	Tungsten Carbide	10:1	300	25	[22]
Fe, Ni, Cr, Mo, Al and Mn	Stainless Steel	30:1	500	16	[23]
Fe, Cr, Ni, W and Ti	Stainless Steel	10:1	380	60	[24]
Fe, Cr, W, Fe-Ti and Fe-Y	Stainless Steel	8:1	225	100	[25]
Fe, Cr, Mn and Mo	Stainless Steel	25:1	300	60	[26]
Fe, Cr and Mn	Stainless Steel	25:1	300	100	[27]
Fe, Cr and Mn	Stainless Steel	10:1	400	144	[28]
Fe-Cr, Fe-Ni and Fe-Mn	Tungsten Carbide	10:1	300	10	Current study

When compared to stainless steel balls and vials, the kinetic energy of the moving particles within the vial is higher for tungsten carbide due to its higher density. If the austenitic stainless steel powders were to be developed from elemental powders, their evolution would require much more time compared to their development from pre-alloyed mixtures.

3.2. Evaluation of Density for the Hot Pressed Samples

Consolidation of the MA powders was carried out using hot pressing under a vacuum atmosphere. Density measurements for the vacuum hot pressed samples were performed using Archimedes principle. Theoretical density was calculated using rule of mixtures and compared with the hot pressed density as shown in Figure 4. The density attained for the hot pressed samples is averaged to be 7.67 g/cc which is 98.8% the density when compared to the theoretical density. A higher density was achieved due to MA, which fractured the powder particles to produce complicated shapes, which in turn increased the surface area of the powder particles required for hot pressing. Reduction in the size of the particles led to the formation of single compacts during hot pressing through grain boundary diffusion rather than lattice diffusion [29,30]. The high specific area of the powder particles initiated the surface diffusion mechanism during the initial stages of sintering. As the sintering progressed, grain boundary diffusion occurred and during later stages volume diffusion took place to produce highly dense compacts.
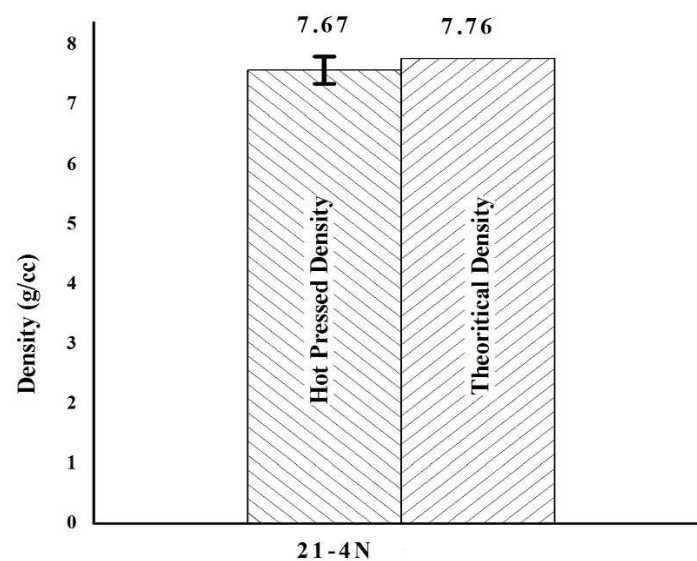
Figure 4. Density of hot pressed samples developed through powder metallurgy route.

3.3. Metallography Analysis

Figure 5a depicts the optical micrograph of 21-4N austenitic steel developed through vacuum hot pressing. The microstructure consists of equiaxed austenitic grains with grain boundary carbides distributed heterogeneously along the grain boundaries. The formation of grain boundary carbides is due to the slow cooling rate of 25 °C/min attained during vacuum hot pressing. The cooling rate plays an important role in the formation of metal carbides in an austenitic structure. This 21-4N alloy consists of low nickel and a high concentration of chromium in the metal matrix. Due to this, the grain boundary carbides consist of chromium-rich precipitates which are seen as dark phases within the micrograph. The light region represents austenitic grains. As the temperature for sintering is high (1200 °C), pores are not evident in the micrograph. Growth of grains did not occur at a faster pace at the beginning stages of sintering. However, at later stages of the sintering, cycle due to high temperatures, the available pores were rounded off. This can be interpreted in relation to a larger grain size in comparison to the crystallite size obtained as a result of MA. The sintering mechanism promotes the volume diffusion process through grain boundaries which act as vacancy sinks. The coalescence of pores occurs at high temperatures where grain growth is observed with grain boundaries as pinning points. Grain growth resulted in the rounding off of pores with little room for vacancies. Similarly, the density of the samples increased due to grain growth as well as volume diffusion.
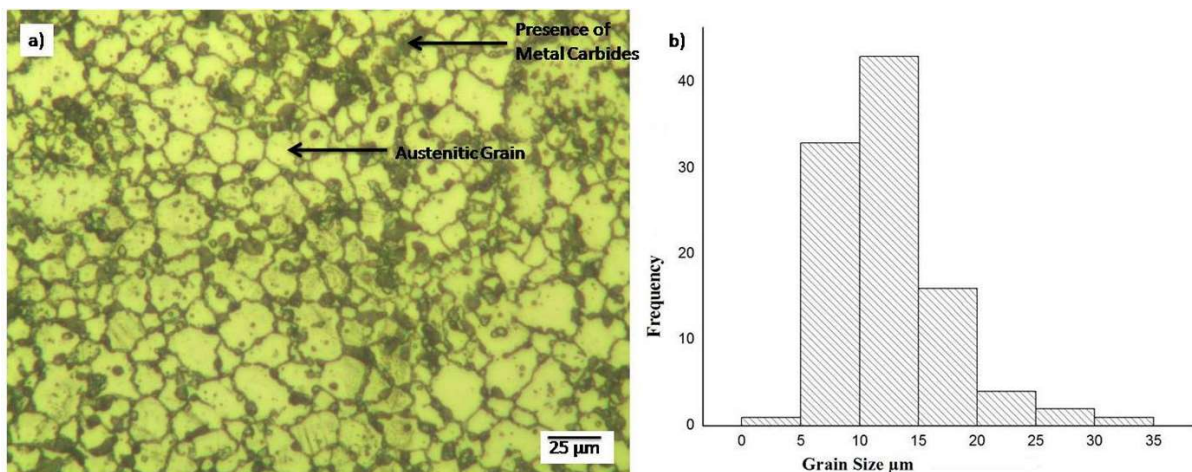

Figure 5. Optical micrograph of (**a**) 21-4N, (**b**) corresponding grain size.

The mean grain size of the austenitic grain was found to be around 7–12 μm as shown in Figure 5b. The grain size was measured using the intercept method as per ASTM E112. The size of the grains was much smaller compared to a similar cast product which contained 16 μm and 17 μm sized grains as reported by Ji et al. and Kumar et al., respectively [20,31]. The initial starting size of the powders followed by the MA inhibited the grain growth during sintering in order to obtain a fine grain size.

The precipitation of carbides along the grain boundaries can still be authenticated using a SEM-EDS analysis. Figure 6a,b show the SEM-EDS analysis of both the grain and grain boundaries of 21-4N austenitic stainless steel. The presence of carbide precipitates is due to the effect of alloying elements within the metal matrix which change the solubility of carbon in the austenitic matrix. As nickel and manganese are austenitic stabilizers, they enhance the precipitation of carbides by reducing their solubility within the metal matrix.
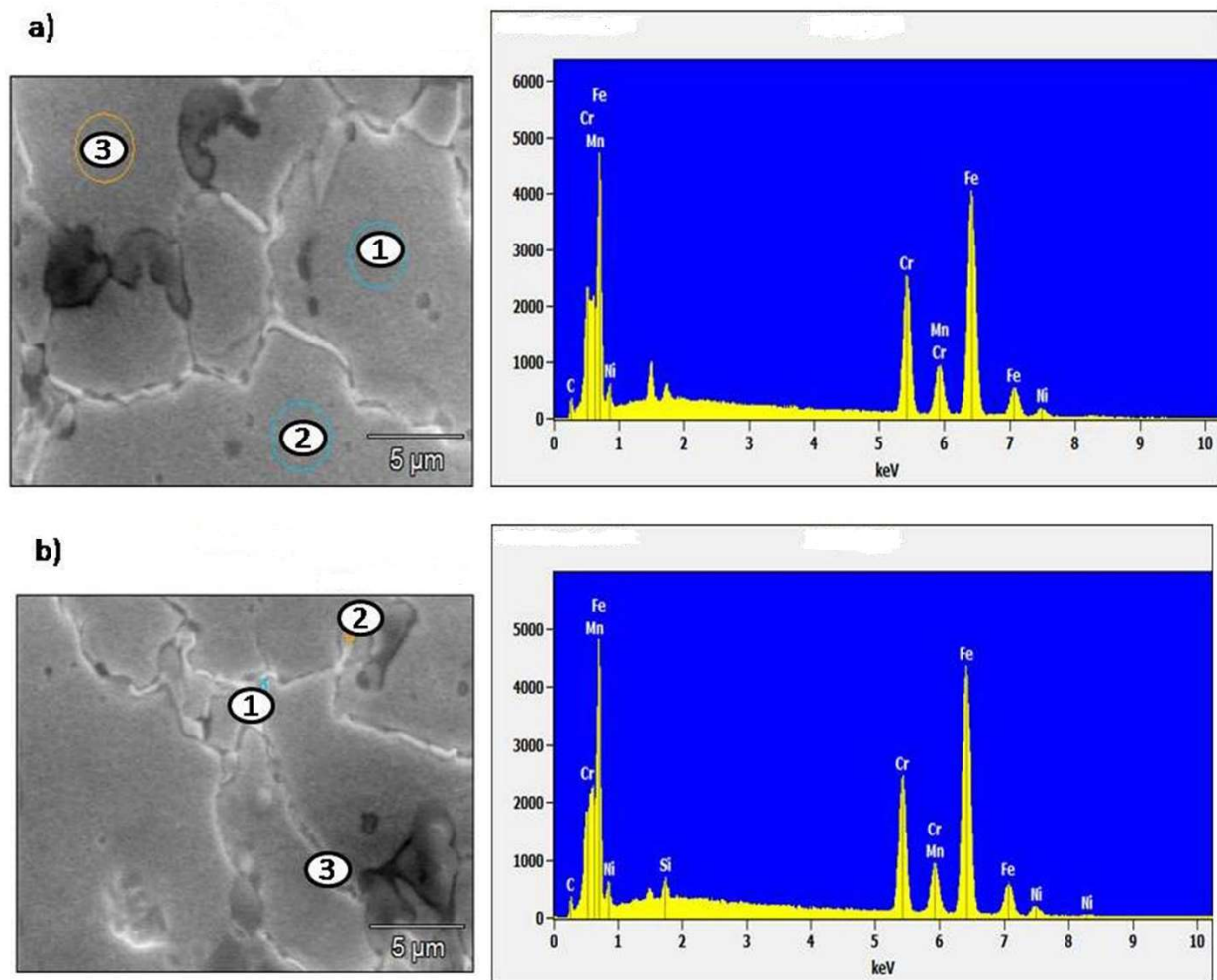
Figure 6. SEM-EDS analysis of 21-4N both at (**a**) grains and (**b**) grain boundaries.

In both the grains and grain boundaries, three sections of EDS measurement were selected and shown in Table 3. A variation in the chemical composition can be seen from the EDS analysis. It is evident that elemental migration took place from the grains to the grain boundary. From Figure 6a, concentration spots (1, 2 and 3) within the grain reveal the presence of an austenite stabilizing element such as nickel at an appropriate level. Similarly, at the grain boundary spot in Figure 6b, a higher concentration (1, 2 and 3) of chromium, carbon and manganese along with iron were found in excess in comparison to the required elemental composition. In comparison to similar studies conducted by Xu et al., the size of the carbide precipitates were not larger or continuously dispersed within the metal matrix [32]. Moreover, the development of the alloy through the powder metallurgy route led to the formation of fine grains and restricted the size of metal carbide precipitates.

Table 3. EDS concentration of elements both at grain boundaries and grains.

Location	Region	Concentration of Elements, wt%				
		Cr	Ni	Mn	C	Fe
Grain	1	19.9	3.8	8.5	0.25	Bal.
	2	19.2	3.6	8.3	0.30	Bal.
	3	18.7	4.1	8.7	0.27	Bal.
Grain Boundary	1	25.3	4.4	9.2	0.65	Bal.
	2	26.4	4.25	9.1	0.70	Bal.
	3	24.2	4.3	8.9	0.68	Bal.

The XRD analysis of the vacuum hot pressed steel is shown in Figure 7, and it can be confirmed that these metal carbides were mostly composed of $M_{23}C_6$ where M represents chromium, manganese and iron. The formation of carbides occurred mainly due to the higher C/Cr ratio. From the metallographic studies, it can be understood that $M_{23}C_6$ nucleates very easily at the beginning when compared to other types of carbides. Moreover, the structural shape of these metal carbides is of a globular or cellular type. These carbide precipitates are usually observed near the grain boundaries due to it being a favorable place for carbon, with an interstitial solid solution capability which rapidly diffuses near the grain boundaries. The intensity of austenite peaks was dominant when compared to $M_{23}C_6$ peaks. The formation of the $M_{23}C_6$ peak in hot pressed samples is due to slow cooling in the sintering cycle. During the sintering of MA powders at 1200 °C, the peaks of austenite became intense and sharper with diminished peaks of $M_{23}C_6$. The presence of $M_{23}C_6$ at the grain boundary improved the material resistance to heat and sliding of grains. Similarly, Figure 8 shows the XRD analysis of powder particles milled for 10 h. The austenitic peak is evident from the XRD analysis.
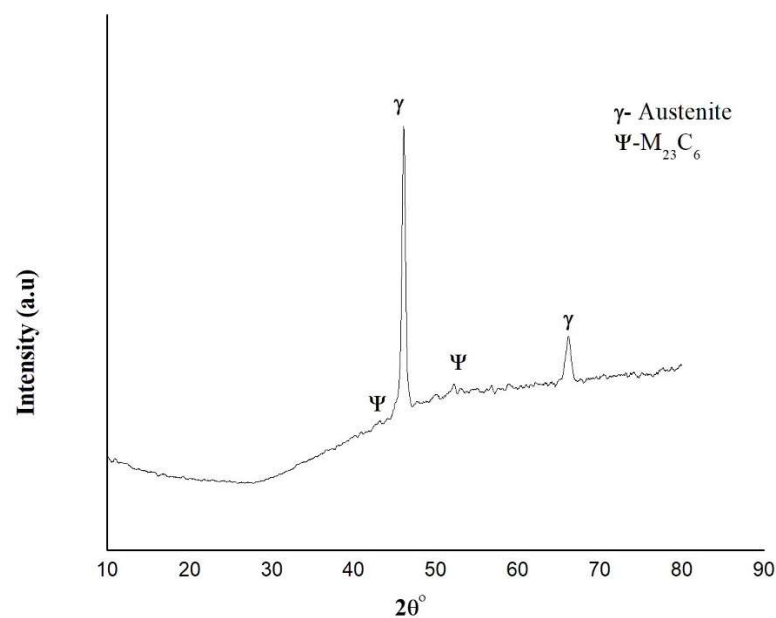
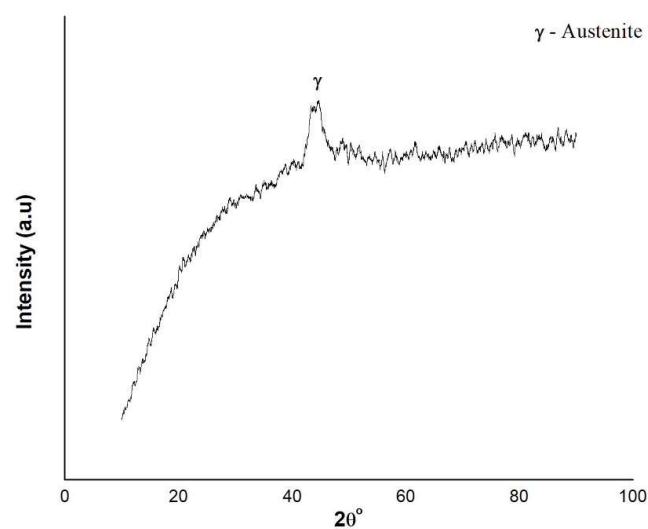**Figure 7.** X-ray diffraction pattern for vacuum hot pressed sample.

Figure 8. X-ray diffraction pattern for milled powder.

Figure 9a represents the TEM microstructure of the vacuum hot pressed steel. Within the austenitic grain, twins were available which indicates the presence of an austenitic matrix. Face centered cubic crystal alloys have a tendency to form twins within the microstructure when subjected to cold working and annealing as a result of low stacking fault energy. Due to low stacking faults, the energy required for twin formation is lower when compared to grain boundary formation. These kinds of fine austenitic twins are found as the material is subjected to cold working and annealing during ball milling and vacuum hot pressing, respectively. Few dislocations were also found within the grains due to hot pressing. The formation of nano crystalline grains along with dislocations is the outcome of severe plastic deformation. The dislocations are pinned at the grain boundaries. This is due to the presence of metal carbides which are present at the grain boundaries that resist dislocation due to the precipitate strengthening mechanism. These precipitates will impede movement or dislocation and resists plastic deformation. Due to MA, the powders consists of residual stresses which act as sites for nucleation [33]. During sintering, these powders nucleates and give rise to the particle stimulated nucleation phenomenon. Face centered cubic structures are found to have particle stimulated nucleation. As the holding time during sintering is 2 h, some grains nucleate near the grain boundaries. This is because a favorable place for grain nucleation is near the grain boundaries which are also the locations for rapid diffusion when compared to a lattice. From Figure 9a, few grains are seen in between the grain and grain boundary region. Grain sizes of the TEM samples were determined by the method of linear intercept. The mean grain size of 1 μm was obtained for the samples developed through vacuum hot pressing as shown in Figure 9b. Cast products with similar compositions had large precipitates of carbides along with σ-phases which were not visible near the grain boundary in the current study [3]. Due to the particle stimulated nucleation phenomenon, very few residual carbides were seen within the metal matrix along with the formation of grains and grain boundaries. Similarly, as the material was manufactured using MA and subsequently consolidated using hot pressing, σ-phases and other intermetallics were not visible as sintering took place under a vacuum atmosphere. The selected area diffraction (SAD) pattern, as shown in Figure 9c, indicates the formation of a nanocrystalline structure even after the consolidation of MA powders at 1200 °C. The rings represent the formation of nano crystallite structures of the metal matrix. Correspondingly, the outer ring represents the formation of face centered cubic structures, namely (111) and (222), respectively. Both the austenitic matrix and precipitates of the carbides co-exist within the metal matrix due to the fact that both have face centered cubic structures.
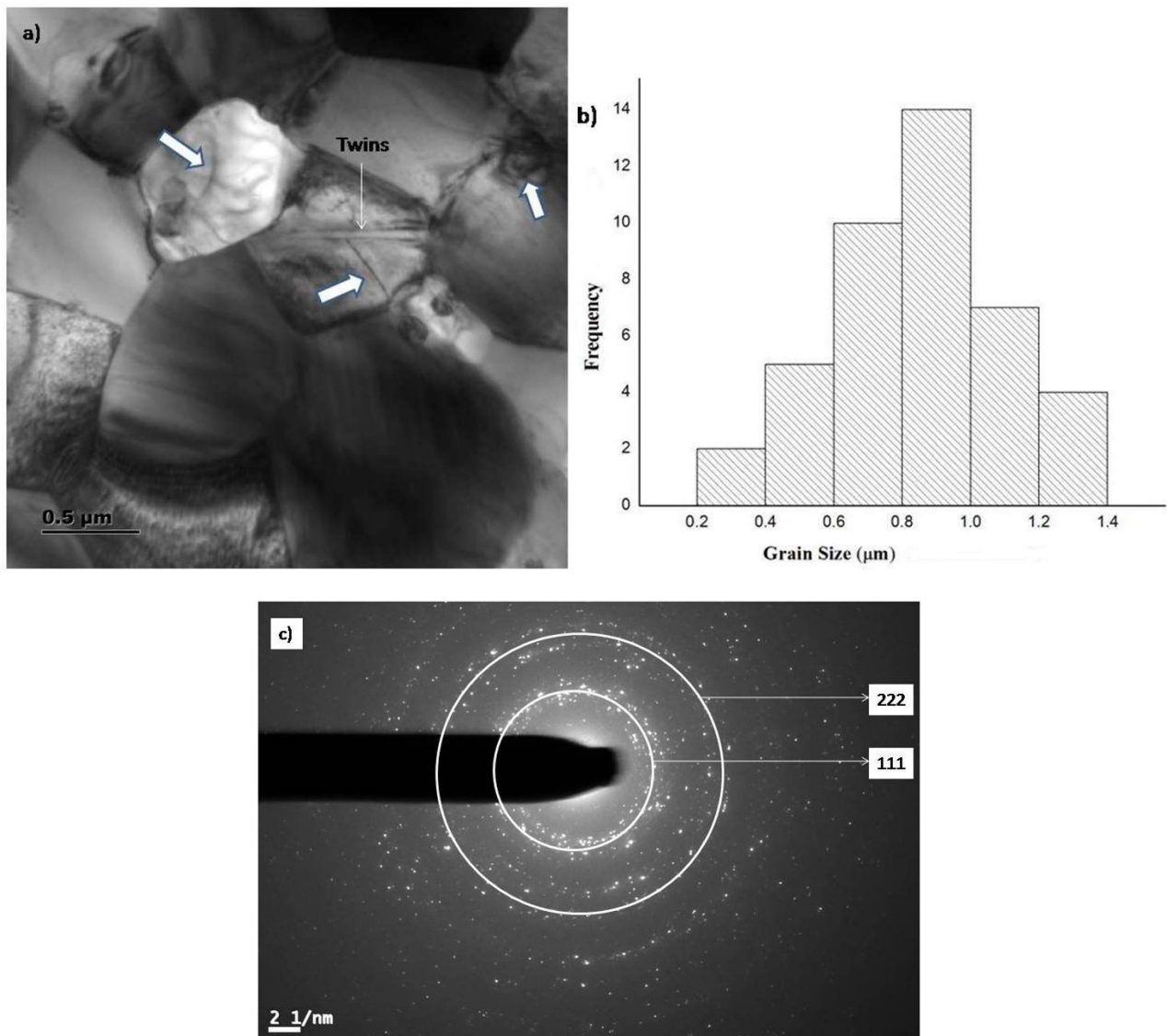
Figure 9. TEM micrograph of heat resistant austenitic steel of 21-4N (**a**) bright field image where arrow mark indicates dislocation lines, (**b**) distribution of grain size for the austenitic matrix, (**c**) corresponding SAD pattern.

3.4. Hardness Measurement

Measurement of hardness was carried out using Vickers microhardness. Table 4 shows the hardness value in comparison with other 21-4N heat-resistance steels manufactured through other processing routes. The hardness obtained through the powder metallurgy process was higher when compared to the hardness obtained through other processing techniques. The increase in hardness is due to the higher sintering temperature during the vacuum hot pressing technique [34]. Moreover, it can be seen that the presence of nano crystalline structures led to the formation of a fine-grained metal matrix which was evident from the microstructural analysis from Figure 9b which resulted in superior hardness for the alternate valve steel material developed using the powder metallurgy route. Similarly, the availability of precipitate strengthened metal carbides distributed heterogeneously (not as continuous structure) near the grain boundaries which had a significant effect on the increase in hardness. This acted as a strengthening mechanism in the formation of precipitates.

Table 4. Comparison of hardness values obtained for different valve steel made of 21-4N material.

Sl No.	Manufacturing Method	Hardness Value (Hv)	References
1	Casting	360 ± 15	[3]
2	Casting	320 ± 10	[35]
3	Casting	290 ± 10	[4]
4	Casting	375 ± 15	[36]
5	Hot rolled	343	[31]
6	Powder Metallurgy	410 ± 10	Present Study

3.5. Hot Compression Measurements

Figure 10 represents high temperature compression stress strain curves for 21-4N steel at 650 °C and 0.001 s^{-1}. Superior strength of 1340 MPa was reported for the material developed using the powder metallurgy technique. The flow stress hump that can be seen within the compressive stress strain graph is due to the formation of dynamic recrystallization which accumulates during the straining [37]. Figure 11a illustrates the micrograph of hot compressed samples at a temperature 650 °C and strain rate of 0.001 s^{-1}. Local bulging along with serrated irregular boundaries are indicated by arrow marks from Figure 11b. In the SEM micrograph, the serrated irregular boundaries are due to the movement of dislocations near the regions. Due to the fine microstructure, shearing of the particles is avoided, leaving behind deformations in the form of bulging. Similarly, near the serrated boundaries the structure consists of early stages of recrystallization. When compared to the compression test of the 21-4N cast product, steel developed through the powder metallurgy route showed higher compressive strength with a higher strain rate. Materials developed through cast products showed a decreasing trend in hot compressive strength. Huang et al., reported a maximum hot compressive stress value of 350 MPa with material developed through cast product [38]. Similar results of 350 MPa were reported by Li et al., and Ji et al., for 21-4N material developed through the cast process [19,20]. This can be attributed to the fact that inhomogeneous distribution of grain growth from the surface to inner layers occurred during uneven solidification rate. The development of the homogeneous and fine microstructure attained as a result of the powder metallurgy processing route showed substantial improvement in hot compressive values when compared to materials processed using the cast route.
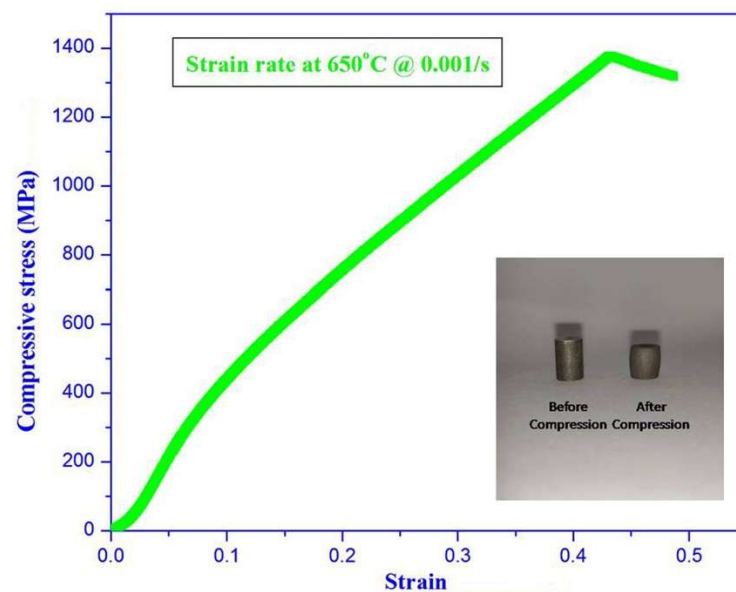
Figure 10. Hot compressive strength of the sintered sample, sample before and after compression (insert).
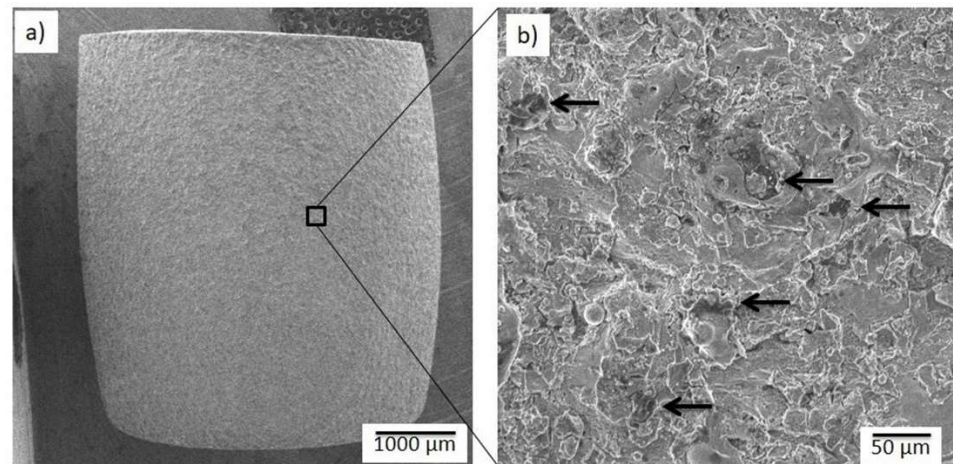
Figure 11. SEM micrograph of hot compressed sample (**a**) Overview of bulged sample (**b**) indication of serrated boundaries.

3.6. Corresponding Relationship between Mechanical and Microstructural Properties

The strength of the material at room temperatures was calculated and compared with the strengthening mechanism. As stated in Equation (1), the strength of the material at room temperatures was obtained with hardness measurements, where *Hv* is the value of the obtained hardness in terms of MPa and σ_y is the yield strength [39]. A multiplication factor of 9.8065 was used to convert the obtained hardness from Hv to MPa [40]. The value of yield stress as per Equation (1) is 1340 MPa.

$$\sigma_y = \frac{1}{3}H_v \tag{1}$$

For any alloy, the calculation of yield strength is also based on the combined contribution of the various strengthening mechanisms as stated in Equation (2) [39].

$$\sigma_y = \sigma_{ss} + \sigma_{gs} + \sigma_{dis} \tag{2}$$

where σ_{ss} is strengthening due to a solid solution, σ_{gs} is grain size strengthening and σ_{dis} strengthening due to dislocations. The effect of solid solution strengthening in an alloy is mainly due to both substitutional and interstitial types of elements present in the system. In the present study, substitutional elements consisted of chromium, nickel and manganese which were the major alloying elements. Meanwhile, the presence of interstitial or minor alloying elements based on their wt% was neglected, which in this case was carbon. The solvent iron which is strengthened due to substitutional elements is given by Equation (3) [41].

$$\sigma_{ss} = 0.00689KX^n \tag{3}$$

where "*K*" is coefficient of strengthening and the corresponding values of "*K*" for the elements chromium, nickel and manganese are 1400, 6100 and 7000, respectively, "*X*" represents the elemental concentration in the present alloy in terms of atomic percentage and "*n*" is the constant valued 0.75 [42]. The effect of strengthening due of solid solution for the current study is found to be 447 MPa from Equation (3). The Hall Petch relation can be used to calculate the strengthening effect as a result of fine grain structure as per Equation (4).

$$\sigma_{gs} = \sigma_o + kd^{\frac{-1}{2}} \tag{4}$$

where "σ_o" is taken as 30 MPa for iron alloys which is known as friction stress, "*k*" is a constant and taken as 0.4 MN/m^2 for austenitic stainless steel grain sizes of less than 3 μm and "d" is the grain size (in meters) for the alloy [43]. Taking the average grain size of the

samples from Figure 9b as 1 μm, the yield strength due to grain boundary strengthening is 430 MPa. The increase in strength due to dislocations present in the alloy is calculated using Equation (5) [44].

$$\sigma_{dis} = \alpha M G b \sqrt{\rho} \tag{5}$$

The efficiency of the hardening effect induced due to dislocation is denoted by "α" which as a constant ranges from 0.1 to 0.5, where the mean value is taken for calculation [42]. For a given FCC structure, "M" denotes Taylor's factor which is 3, "G" is termed as modulus of rigidity and for pure iron it is 83 GPa, "b" is burgers vector and for the FCC material it is 0.251 nm. Dislocation density for the vacuum hot pressed samples is expressed as "ρ" and is taken as 5×10^{14} m^{-2} [45]. From Equation (5), as a result of dislocation strengthening, the yield strength is 419 Mpa. From Equation (2) the overall yield strength obtained from the strengthening mechanisms, namely solid solution strengthening, grain size strengthening and dislocation strengthening can be found to be 1296 MPa. The obtained theoretical value as per Equation (1) is slightly overestimated by 3.39% which is in good agreement with the summation of all contributed strengthening mechanisms. The overestimated observation is due to either the summation or overestimation of individual strengthening contributions. Alloys consisting of solid solution strengthening lead to overestimation as a result of friction stress. The factor of friction stress is dependent on temperature, dislocation and slip system. Chauhan et al. reported that when comparing the calculated and measured values of yield stress, a small amount of overestimation for all alloys up to 53 Mpa occurs, whereas smaller values of 30 MPa were also reported by Li [42,46].

4. Conclusions

The current study reported on the development and evaluation of mechanical and microstructural properties of 21-4N austenitic steel through the powder metallurgy route. Parameters used for sintering gave rise to a balanced austenitic structure when compared to cast products with a similar composition. The 21-4N austenitic valve steel developed through MA to obtain a nano-crystalline structure led to the following conclusions.

During the initial stages of milling, pre-alloyed mixtures were soft and ductile. A prolonged milling time leads to the cold welding of particles and break down due to repeated fracturing. The morphology of the milled powders revealed that the fracturing of powder particles was dominant when compared to cold welding.

MA powders were consolidated using vacuum hot pressing which had a density of 98% in comparison to the theoretical density of the samples. High dense samples were obtained due to grain boundary diffusion and volume diffusion during sintering.

SEM-EDS studies revealed the presence of carbide precipitates near the grain boundaries. XRD analysis of the hot pressed samples confirmed the precipitates as $M_{23}C_6$, whereas these precipitates were not present in the powder particle. The formation of $M_{23}C_6$ carbide particle is due to slow cooling in the sintering cycle.

The TEM analysis revealed the presence of austenitic twins as materials were subjected to cold working and annealing. Dislocations were present within the metal matrix as an outcome of severe plastic deformation which is due to hot pressing. A fine grain structure was revealed during the TEM analysis with a mean grain size is of 1 μm.

When compared to other conventional processing techniques, the hardness value of 410 ± 10 Hv obtained through the powder metallurgy route was higher. The presence of a nano crystalline structure led to an increase in the hardness value. Evaluations of the strengthening mechanism clearly reveal that strengthening due to solid solution, grain size and dislocations are the dominant forces which increase the structural rigidity of the alloy.

Substantial improvements in the hot compression value of 1340 MPa were reported for 21-4N austenitic valve steel when compared to similar material developed through the cast product technique. The development of fine microstructure throughout the material resulted in the increase in hot compression values.

With the obtained results, 21-4N austenitic valve steel developed through the powder metallurgy route was demonstrated to have better strength and structural rigidity for the metal matrix which can be used for high temperature applications.

Author Contributions: Conceptualization and methodology, A.P.M. and D.G.; writing—original draft preparation, A.P.M. and D.G.; writing—review and editing, S.S., E.A.N., H.M.A.H. and J.P.D. All authors have read and agreed to the published version of the manuscript.

Institutional Review Board Statement: Not applicable.

Informed Consent Statement: Not applicable.

Data Availability Statement: Not applicable.

Conflicts of Interest: The authors declare no conflict of interest.

References

1. *ASM Handbook: Properties and Selection: Nonferrous Alloys and Special-Purpose Materials*; ASM International: Novelty, OH, USA, 1991; Volume 2.
2. Badami, M.; Marino, F. Fatigue tests of un-HIP'ed γ-TiAl engine valves for motorcycles. *Int. J. Fatigue* **2006**, *28*, 722–732. [CrossRef]
3. Choi, J.; Seok, C.S.; Park, S.; Kim, G. Effect of high-temperature degradation on microstructure evolution and mechanical properties of austenitic heat-resistant steel. *J. Mater. Res. Technol.* **2019**, *8*, 2011–2020. [CrossRef]
4. Witek, L. Failure and thermo-mechanical stress analysis of the exhaust valve of diesel engine. *Eng. Fail. Anal.* **2016**, *66*, 154–165. [CrossRef]
5. Zhang, Q.; Zuo, Z.; Liu, J. Failure analysis of a diesel engine cylinder head based on finite element method. *Eng. Fail. Anal.* **2013**, *34*, 51–58. [CrossRef]
6. Raghuwanshi, N.K.; Pandey, A.; Mandloi, R. Failure analysis of internal combustion engine valves: A review. *Int. J. Innov. Res. Sci. Eng. Technol.* **2012**, *1*, 173–181.
7. Hasan, M.R. Failure Investigation Report on Different Components of an Automotive Engine. *Int. J. Mech. Eng. Appl.* **2017**, *5*, 47–51.
8. Yu, Z.; Xu, X. Failure analysis and metallurgical investigation of diesel engine exhaust valves. *Eng. Fail. Anal.* **2006**, *13*, 673–682. [CrossRef]
9. Kum-Chul, O.; Sang-Woo, C.; Ji-Ho, K. A study of durability analysis methodology for engine valve considering head thermal deformation and dynamic behavior. In Proceedings of the SIMULIA Community Conference, Corp Providence, RI, USA, 19–22 May 2014.
10. Ivasishin, O.M.; Anokhin, V.M.; Demidik, A.N.; Savvakin, D.G. Cost-effective blended elemental powder metallurgy of titanium alloys for transportation application. In *Key Engineering Materials*; Trans Tech Publications: Freienbach, Switzerland, 2000.
11. Şap, E.; Usca, U.A.; Gupta, M.K.; Kuntoğlu, M. Tool wear and machinability investigations in dry turning of Cu/Mo-SiCp hybrid composites. *Int. J. Adv. Manuf. Technol.* **2021**, *114*, 379–396. [CrossRef]
12. M'Saoubi, R.; Czotscher, T.; Andersson, O.; Meyer, D. Machinability of powder metallurgy steels using PcBN inserts. *Procedia CIRP* **2014**, *14*, 83–88. [CrossRef]
13. Kurita, H.; Miyazaki, T.; Kawasaki, A.; Lu, Y.; Silvain, J.F. Interfacial microstructure of graphite flake reinforced aluminum matrix composites fabricated via hot pressing. *Compos. Part A Appl. Sci. Manuf.* **2015**, *73*, 125–131. [CrossRef]
14. Bartolomeu, F.; Buciumeanu, M.; Pinto, E.; Alves, N.; Carvalho, O.; Silva, F.S.; Miranda, G. 316L stainless steel mechanical and tribological behavior—A comparison between selective laser melting, hot pressing and conventional casting. *Addit. Manuf.* **2017**, *16*, 81–89. [CrossRef]
15. Garbacz, H.; Mizera, J.; Laskowski, Z.; Gierej, M. Microstructure and mechanical properties of a Pt–Rh alloy produced by powder metallurgy and subjected to plastic working. *Powder Technol.* **2011**, *208*, 488–490. [CrossRef]

16. Moravcikova-Gouvea, L.; Moravcik, I.; Omasta, M.; Veselý, J.; Cizek, J.; Minárik, P.; Cupera, J.; Záděra, A.; Jan, V.; Dlouhy, I. High-strength Al0. 2Co1. 5CrFeNi1. 5Ti high-entropy alloy produced by powder metallurgy and casting: A comparison of microstructures, mechanical and tribological properties. *Mater. Charact.* **2020**, *159*, 110046.

17. Schaffer, G. Powder processed aluminium alloys. *Mater. Forum* **2004**, *28*, 65–74.

18. Li, Y.; Ji, H.; Cai, Z.; Tang, X.; Li, Y.; Liu, J. Comparative study on constitutive models for 21-4N heat resistant steel during high temperature deformation. *Materials* **2019**, *12*, 893. [CrossRef]

19. Li, Y.; Ji, H.; Li, W.; Li, Y.; Pei, W.; Liu, J. Hot deformation characteristics—Constitutive equation and processing maps—of 21-4N heat-resistant steel. *Materials* **2019**, *12*, 89. [CrossRef]

20. Ji, H.; Huang, X.; Ma, C.; Pei, W.; Liu, J.; Wang, B. Predicting the microstructure of a valve head during the hot forging of steel 21-4N. *Metals* **2018**, *8*, 391. [CrossRef]

21. Wang, M.; Sun, H.; Zou, L.; Zhang, G.; Li, S.; Zhou, Z. Structural evolution of oxide dispersion strengthened austenitic powders during mechanical alloying and subsequent consolidation. *Powder Technol.* **2015**, *272*, 309–315. [CrossRef]

22. Susila, P.; Sturm, D.; Heilmaier, M.; Murty, B.S.; Subramanya Sarma, V. Microstructural studies on nanocrystalline oxide dispersion strengthened austenitic (Fe–18Cr–8Ni–2W–0.25Y2O3) alloy synthesized by high energy ball milling and vacuum hot pressing. *J. Mater. Sci.* **2010**, *45*, 4858–4865.

23. Phaniraj, M.P.; Kim, D.I.; Shim, J.H.; Cho, Y.W. Microstructure development in mechanically alloyed yttria dispersed austenitic steels. *Acta Mater.* **2009**, *57*, 1856–1864. [CrossRef]

24. Xu, Y.; Zhou, Z.; Li, M.; He, P. Fabrication and characterization of ODS austenitic steels. *J. Nucl. Mater.* **2011**, *417*, 283–285. [CrossRef]

25. Liu, D.H.; Yong, L.I.U.; Zhao, D.P.; Yan, W.; Fang, J.H.; Wen, Y.R.; Liu, Z.M. Effect of ball milling time on microstructures and mechanical properties of mechanically-alloyed iron-based materials. *Trans. Nonferrous Met. Soc. China* **2010**, *20*, 831–838. [CrossRef]

26. Tehrani, F.; Golozar, M.A.; Abbasi, M.H.; Panjepour, M. Characterization of nanostructured high nitrogen Fe–18Cr–xMn–4Mo austenitic stainless steel prepared by mechanical alloying. *Mater. Sci. Eng. A* **2012**, *534*, 203–208. [CrossRef]

27. Haghir, T.; Abbasi, M.H.; Golozar, M.A.; Panjepour, M. Investigation of α to γ transformation in the production of a nanostructured high-nitrogen austenitic stainless steel powder via mechanical alloying. *Mater. Sci. Eng. A* **2009**, *507*, 144–148. [CrossRef]

28. Amini, R.; Hadianfard, M.J.; Salahinejad, E.; Marasi, M.; Sritharan, T. Microstructural phase evaluation of high-nitrogen Fe–Cr–Mn alloy powders synthesized by the mechanical alloying process. *J. Mater. Sci.* **2009**, *44*, 136–148. [CrossRef]

29. Liu, D.; Xiong, Y.; Topping, T.D.; Zhou, Y.; Haines, C.; Paras, J.; Martin, D.; Kapoor, D.; Schoenung, J.M.; Lavernia, E.J. Spark plasma sintering of cryomilled nanocrystalline Al alloy-Part II: Influence of processing conditions on densification and properties. *Metall. Mater. Trans. A* **2012**, *43*, 340–350. [CrossRef]

30. Solay Anand, S.; Mohan, B. Effect of particle size, compaction pressure on density and mechanical properties of elemental 6061Al alloy through powder metallurgical process. *Int. J. Mater. Eng. Innov.* **2012**, *3*, 259–268. [CrossRef]

31. Kumar, N.; Arora, N.; Goel, S. Study on metallurgical and mechanical aspects of GMA welded nitronic steel under the influence of weld quenching. *J. Manuf. Processes* **2020**, *56*, 116–130. [CrossRef]

32. Xu, X.; Yu, Z.; Wang, J. Influences of microstructure on service properties of 5Cr21Mn9Ni4N heat resistant alloy. *Mater. Sci. Technol.* **2007**, *23*, 903–909. [CrossRef]

33. Weisser, M.A. Effect of Different Loading Conditions on the Accumulation of Residual Strain in a Creep Resistant 1% CrMoV Steel. Ph.D. Thesis, École Polytechnique Fédérale de Lausanne, Lausanne, Switzerland, 2013.

34. Ganesan, D.; Sellamuthu, P.; Prashanth, K.G. Vacuum Hot Pressing of Oxide Dispersion Strengthened Ferritic Stainless Steels: Effect of Al Addition on the Microstructure and Properties. *J. Manuf. Mater. Processing* **2020**, *4*, 93. [CrossRef]

35. Sato, K.; Saka, T.; Ohno, T.; Kageyama, K.; Sato, K.; Noda, T.; Okabe, M. *Development of Low-Nickel Superalloys for Exhaust Valves*; SAE Technical Paper; SAE: Warrendale, PA, USA, 1998.

36. Kumar, N.; Arora, N. Effect of solution treatment on slurry erosive wear performance of martensitic and nitrogen strengthened austenitic stainless steel. *Mater. Lett.* **2021**, *284*, 128932. [CrossRef]

37. Kunitskaya, I.; Spektor, Y.I.; Olshanetskii, V. Structural and kinetic features of dynamic recrystallization of alloyed austenite upon multipass hot deformation. *Met. Sci. Heat Treat.* **2012**, *53*, 498–502. [CrossRef]

38. Huang, X.; Wang, B.; Zang, Y.; Ji, H.; Guan, B.; Li, Y.; Tang, X. Constitutive relationships of 21-4 N heat-resistant steel for the hot forging process. *J. Mater. Res. Technol.* **2020**, *9*, 13575–13593. [CrossRef]

39. Srinivasan, D.; Corderman, R.; Subramanian, P. Strengthening mechanisms (via hardness analysis) in nanocrystalline NiCr with nanoscaled Y2O3 and Al2O3 dispersoids. *Mater. Sci. Eng. A* **2006**, *416*, 211–218. [CrossRef]

40. Broitman, E. Indentation hardness measurements at macro-, micro-, and nanoscale: A critical overview. *Tribol. Lett.* **2017**, *65*, 1–18. [CrossRef]

41. Lacy, C.; Gensamer, M. The tensile properties of alloyed ferrites. *Trans. AsM* **1944**, *32*, 88–110.

42. Chauhan, A.; Bergner, F.; Etienne, A.; Aktaa, J.; De Carlan, Y.; Heintze, C.; Litvinov, D.; Hernandez-Mayoral, M.; Oñorbe, E.; Radiguet, B.; et al. Microstructure characterization and strengthening mechanisms of oxide dispersion strengthened (ODS) Fe-9% Cr and Fe-14% Cr extruded bars. *J. Nucl. Mater.* **2017**, *495*, 6–19. [CrossRef]

43. Rajasekhara, S.; Ferreira, P.J.; Karjalainen, L.P.; Kyröläinen, A. Hall–Petch behavior in ultra-fine-grained AISI 301LN stainless steel. *Metall. Mater. Trans. A* **2007**, *38*, 1202–1210. [CrossRef]

44.   Praud, M.; Mompiou, F.; Malaplate, J.; Caillard, D.; Garnier, J.; Steckmeyer, A.; Fournier, B. Study of the deformation mechanisms in a Fe–14% Cr ODS alloy. *J. Nucl. Mater.* **2012**, *428*, 90–97. [CrossRef]
45.   Hin, C.; Wirth, B.D. Formation of Y_2O_3 nanoclusters in nano-structured ferritic alloys: Modeling of precipitation kinetics and yield strength. *J. Nucl. Mater.* **2010**, *402*, 30–37. [CrossRef]
46.   Li, Q. Modeling the microstructure–mechanical property relationship for a 12Cr–2W–V–Mo–Ni power plant steel. *Mater. Sci. Eng. A* **2003**, *361*, 385–391. [CrossRef]